Scripta Materialia 222 (2023) 115053

Contents lists available at ScienceDirect

Scripta Materialia

journal homepage: www.journals.elsevier.com/scripta-materialia

Microstructure and mechanical properties of gas metal arc welded CoCrFeMnNi joints using a 308 stainless steel filler metal

Jiajia Shen [a,*], Rita Gonçalves [a], Yeon Taek Choi [b], J.G. Lopes [a], Jin Yang [c], N. Schell [d], Hyoung Seop Kim [b], J.P. Oliveira [a,e,*]

[a] UNIDEMI, Department of Mechanical and Industrial Engineering, NOVA School of Science and Technology, Universidade NOVA de Lisboa, Caparica 2829-516, Portugal
[b] Graduate Institute of Ferrous Technology, POSTECH (Pohang University of Science and Technology), Pohang 790-794, South Korea
[c] School of Materials Engineering, Shanghai University of Engineering Science, Shanghai 201620, China
[d] Helmholtz-Zentrum Hereon, Institute of Materials Physics, Max-Planck-Str. 1, Geesthacht 21502, Germany
[e] CENIMAT|i3N, Department of Materials Science, School of Science and Technology, NOVA University Lisbon, Caparica, Portugal

ARTICLE INFO

Keywords:
CoCrFeMnNi high entropy alloy
Welding
Solidification
Synchrotron X-ray diffraction
Mechanical properties testing

ABSTRACT

In this paper, gas metal arc welding of a CoCrFeMnNi high entropy alloy was performed using 308 stainless steel filler wire. Electron backscatter diffraction and synchrotron X-ray diffraction were used to determine the microstructural evolution, while microhardness mapping and non-contact digital image correlation were employed to assess the local mechanical response across the welded joints. Further, thermodynamic calculations were implemented to support the understanding of the microstructure evolution. Through a systematic analysis of the microstructure evolution and mechanical properties, it is established a correlation between welding process, microstructure and mechanical properties. Besides, this work lays the foundations for the use of low-cost arc-based welding technologies for successful joining and application of welded joints based on high entropy alloys.

Traditionally, alloy design concepts are focused on using one principal element and then improving the desired properties with relatively minor alloying additions. Cantor et al. [1] and Yeh et al. [2] independently proposed a new alloy design strategy which broke the design barriers of traditional alloys. Nowadays, high entropy alloys are attracting significant interest owing to their attractive and unique properties including strength, thermal stability, wear and oxidation resistance [3–8].

One of the most widely studied high entropy alloys is the FCC single phase CoCrFeMnNi [1,9,10], being considered a potential structural material due to its remarkable mechanical properties over a wide range of temperatures [11].

Welding, as one of the most important metal processing methods for structural materials, is virtually used in any structural engineering application. Thus, coupling the development of new materials and determining their weldability is essential promote them as engineering solutions.

So far, researchers focused on the weldability of CoCrFeMnNi high entropy alloys with fusion-based welding processes, including laser beam welding [12–14], electron beam welding [15,16] and tungsten inert gas welding [17]. Although well performing joints have been obtained, they are mainly limited to similar welding combinations. To further expand its applications in nuclear and aerospace sectors, joining of CoCrFeMnNi high entropy alloys to other base materials or the addition of filler materials to adjust the composition and modify the material microstructure is required.

Research on dissimilar welding involving CoCrFeMnNi high entropy alloys is still recent [18–20]. To fill this gap, CoCrFeMnNi sheets were butt welded using gas metal arc welding with 308 stainless steel filler material. Through a combination of microstructure characterization, thermodynamic modeling and mechanical property assessment, a comprehensive understanding of the microstructure evolution caused by the welding thermal cycle and processing conditions and its effect on of the joint properties was obtained.

1.5 mm thick cold-rolled equiatomic CoCrFeMnNi alloy was used in this work [20]. 60 × 60 mm squares were used for butt joining. Ethanol

* Corresponding authors at: UNIDEMI, Department of Mechanical and Industrial Engineering, NOVA School of Science and Technology, Universidade NOVA de Lisboa, Caparica 2829-516, Portugal.
E-mail addresses: j.shen@campus.fct.unl.pt (J. Shen), jp.oliveira@fct.unl.pt (J.P. Oliveira).

https://doi.org/10.1016/j.scriptamat.2022.115053
Received 26 July 2022; Received in revised form 12 September 2022; Accepted 13 September 2022
Available online 18 September 2022

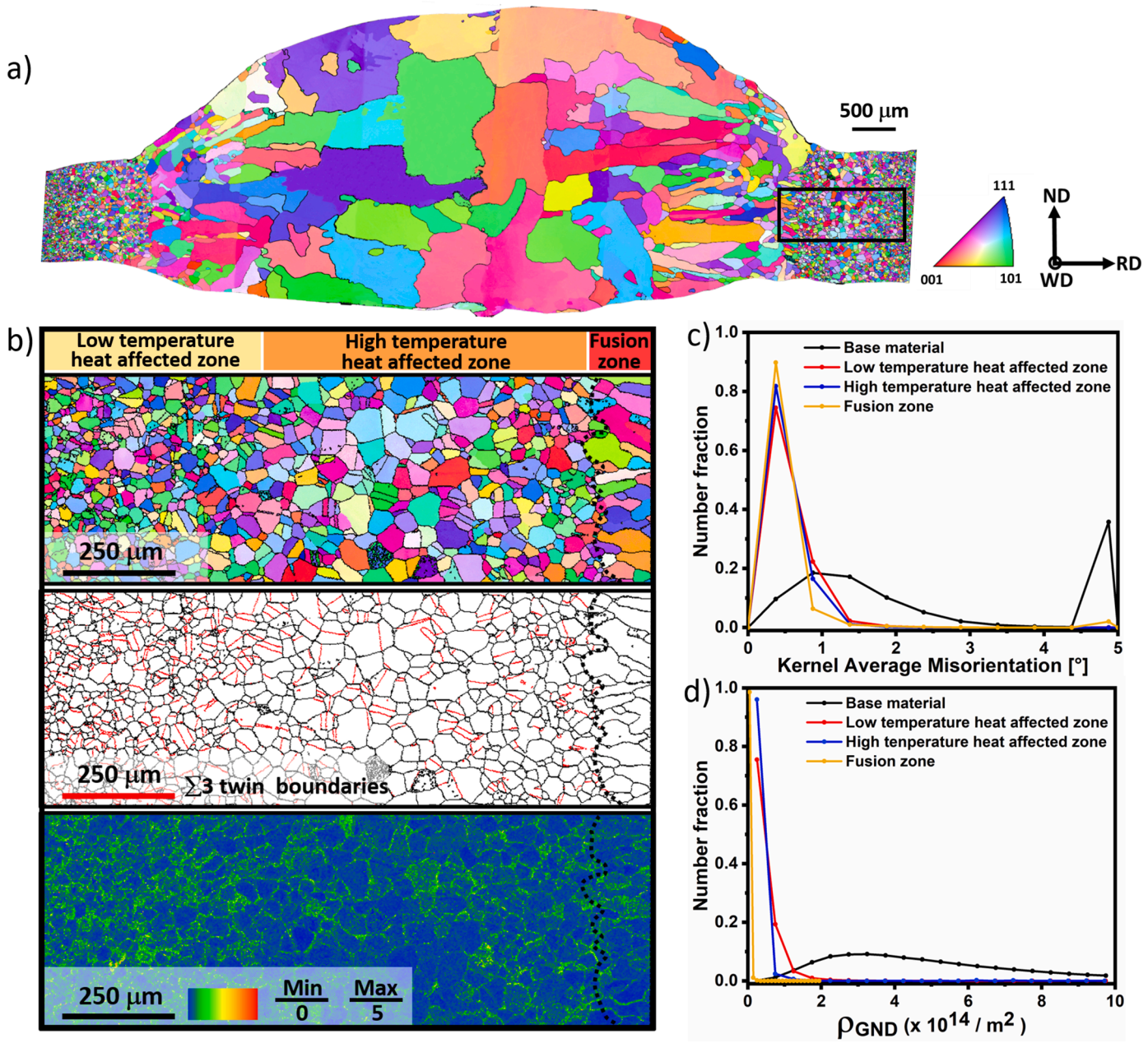

Fig. 1. (a) EBSD map of the gas metal arc welded CoCrFeMnNi joints with ER308LSi filler material; (b) IPF, Σ3 boundaries and KAM (top, middle and bottom, respectively) EBSD maps of the heat affected zone near the base material up to the interface with the fusion zone; (c) and (d) variation of KAM and GND values with respect to the different regions of the joint, respectively.

and alcohol were used to clean the base material before welding.

One key issue during arc-based welding of high entropy alloys is the large hardness drop of the fusion zone due to the presence of a large columnar grain structure. Potentially, the modification of the chemical composition of the fusion zone can aid in minimizing this hardness drop, creating a more homogenous structure. Additionally, chemical control of the fusion zone may modify the solidification temperature range avoiding formation of solidification cracking defects upon cooling.

Gas metal arc welding was used with an austenitic 308LSi stainless steel filler wire. To minimize oxidation, pure Ar at a flow rate of 16 L/min was used as shielding gas. Process optimization led to the following welding parameters: voltage of 18 V, torch travel speed of 185 mm/min and wire feed speed of 2500 mm/min. Specimens were then prepared by electrical discharge machining for microstructural and mechanical characterization.

For microstructural characterization, samples were polished and etched with aqua regia (5 ml HNO_3 and 15 ml HCl). Electron Backscatter Diffraction (EBSD) was performed across the welded joint analysis on a Helios JSM-7100F.

High energy synchrotron X-ray diffraction analysis was used to probe the microstructure across the joints. The experiments were performed at the P07 HEMS beamline of PETRAIII/DESY, with a beam energy of 87.1 KeV. LaB_6 powder was used as standard. Fit2D [21] and MAUD [22] were used for processing the raw diffraction data.

The Scheil-Guliver model was used to predict the number of phases, solidification temperature range, and solidification path of the fusion zone. Steps of 1% dilution were used. A python-based routine was implemented in Thermocalc using the TCHEA5.1 database.

Microhardness testing was conducted on a Mitutoyo HM-112 hardness testing machine with a load of 500 g and an indentation time of 10

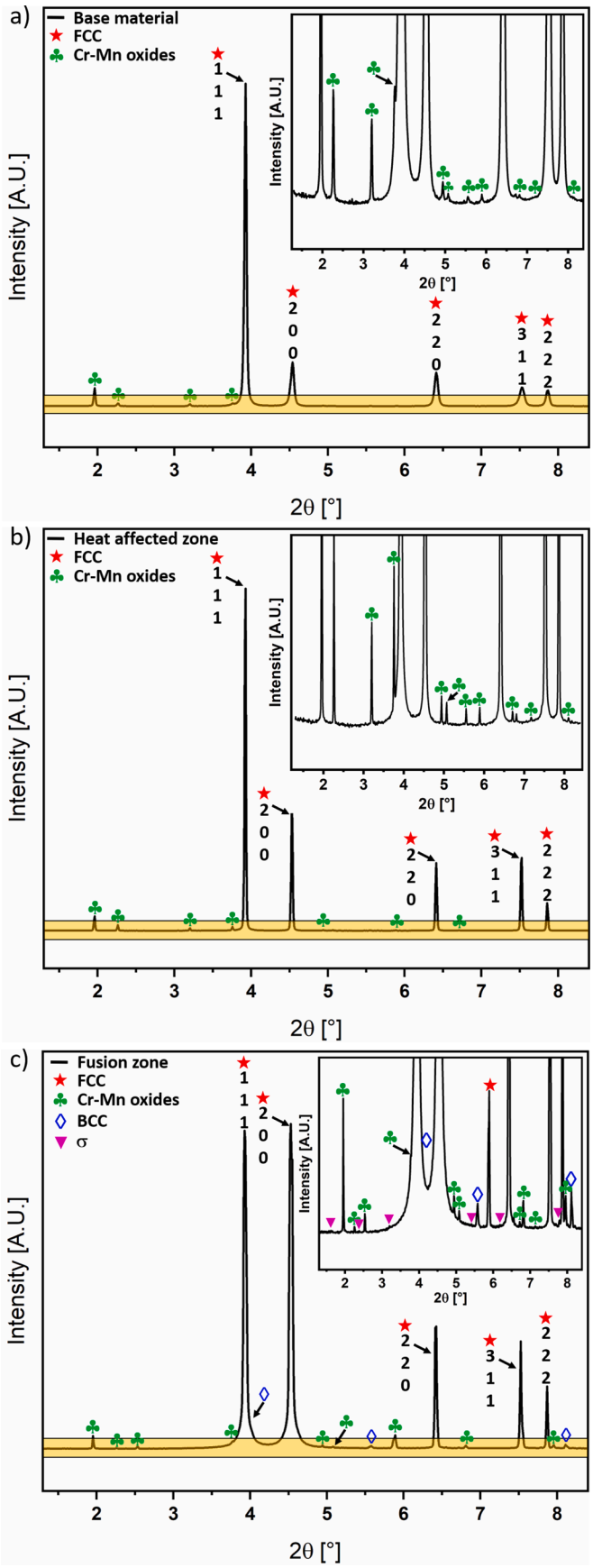

Fig. 2. Representative diffraction patterns from the: (a) base material; (b) heat affected zone; (d) fusion zone. The yellow boxes highlight the inserts used to detail the low intensity peaks captured.

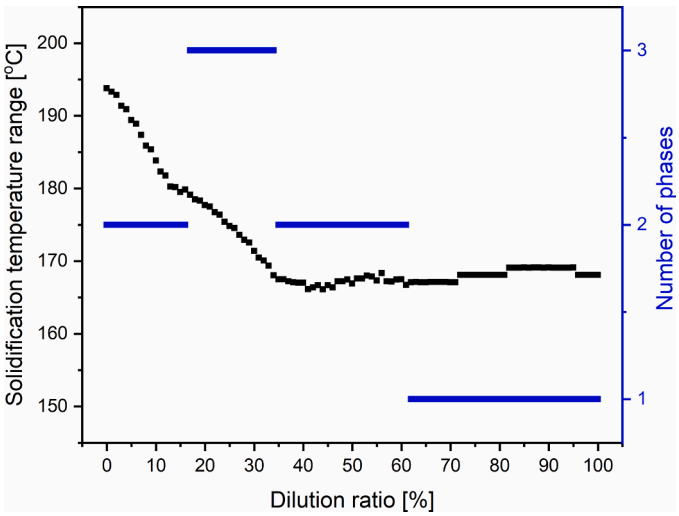

Fig. 3. Thermodynamic calculations performed using the Scheil-Guliver model considering different dilution conditions as a function of number of existing phases at the end of solidification (blue lines) and solidification temperature range (black dots). A 0% dilution ratio corresponds to the 308 stainless steel filler, while a 100% dilution ratio corresponds to the CoCrFeMnNi base material.

s. Room temperature uniaxial tensile tests were performed on a Shimadzu tensile machine, using a strain rate of $1 \times 10^{-3}s^{-1}$. Digital image correlation (DIC) was used during tensile testing to analyze the local stress-strain behavior.

Fig. 1(a) depicts the EBSD map of the joint cross section, detailing a defect-free and full penetration joint. Distinctive microstructural features are observed across the joint, and these are discussed next. The base material experienced cold rolling prior to welding, and the grain structure is composed of pancake-like grains with a width of approximately 2 μm, as previously shown in [23]. Entering the heat affected zone (refer to Fig. 1(b)), the pancake-like grains are replaced by equiaxed grains and the grain size increases to ≈ 15 μm (in the low temperature heat affected zone) and to ≈ 53 μm (in the high temperature heat affected zone). The above changes in microstructure and the coarsening of the grain structure are related to the weld thermal cycle, which resembles the effect of a low and high temperature heat treatment for a short time period. Closer to the base material, i.e., in the low temperature heat affected zone, recovery and recrystallization phenomena are predominant and justify the small equiaxed grains observed at this location. Closer to the fusion zone, i.e., in the high temperature heat affected zone, recrystallization but especially grain growth are the predominant solid-state phenomena, thus in good agreement with the larger grain size observed when approaching the fusion boundary.

Several ∑3 twins were observed in the low temperature heat affected zone (refer to Fig. 1(b), which was induced by a combination of the high prestored strain energy within the base material and the heat imposed to this region of the material during welding. Approaching the fusion boundary, the grain boundaries and annealing twin boundaries move rapidly during the grain growth process, which engulfs the original twin boundaries, leading to a gradual reduction in the fraction of ∑3 twins until they fully disappear upon entering in the fusion zone. Here, fine equiaxed and columnar grains nucleate from the cold substrate (at the heat affected zone/fusion zone interface) with competitive growth towards the weld centerline. Moving away from the cold substrate toward the weld centerline there is preferential formation of coarse columnar grains (refer to Fig. 1(a)), due to the reduction of the temperature gradient, G, to growth rate, R, product. Fig. 1(b) (bottom) reproduces the evolution of the Kernel Average Misorientation (KAM) of the joint, while Fig. 1(c) and (d) detail the KAM and Geometrically Necessary Dislocation (GND) values for different regions across the

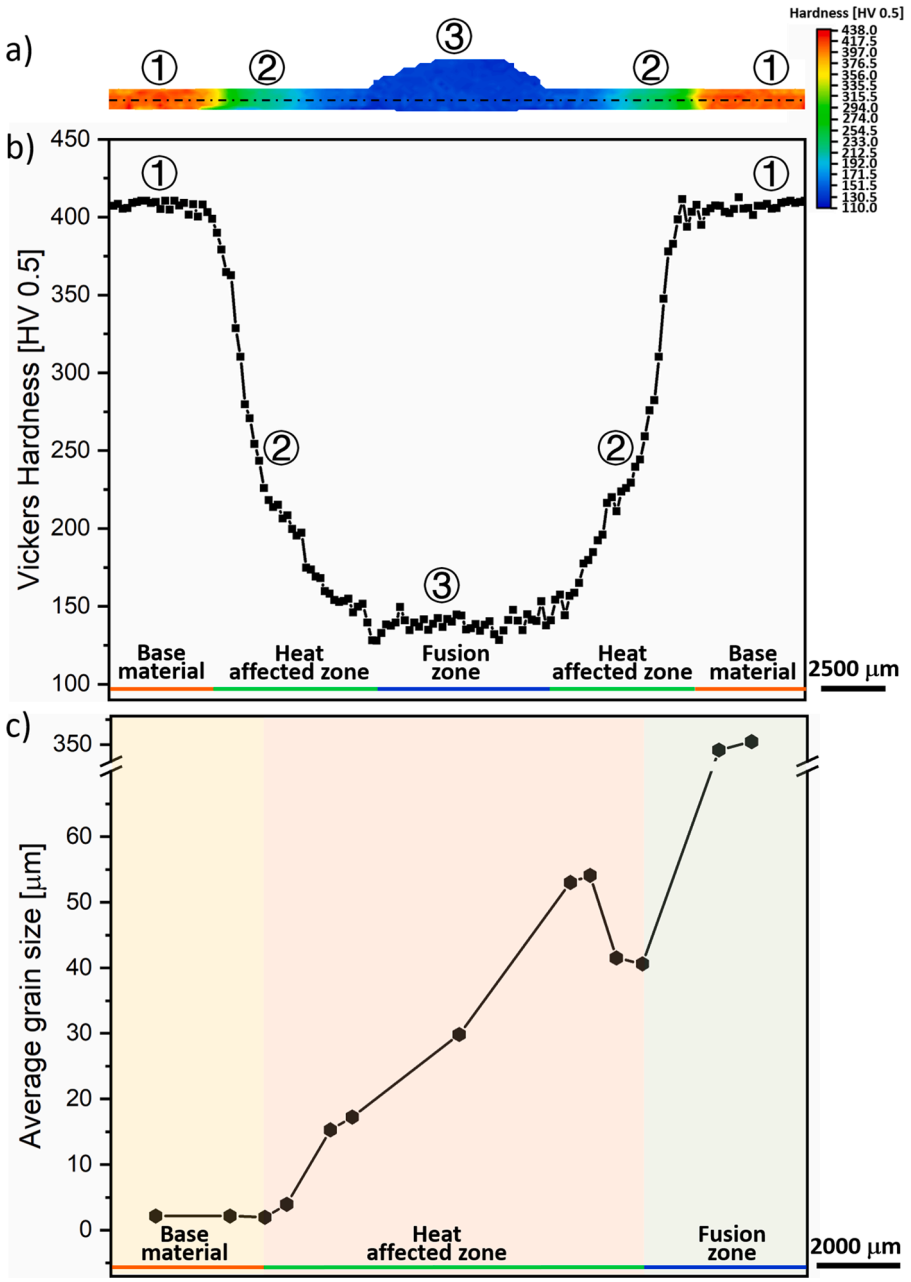

Fig. 4. (a) Microhardness map across the welded joint; (b) microhardness profile obtained at the middle height of the joint (black dashed line in a); (c) average grain size evolution across the joint.

joint. The base material possesses the highest KAM and GND values due to the large plastic deformation resulting from the previously imposed cold rolling. However, upon the introduction of heat during welding, the stored strain energy arising from the cold rolling will aid on the solid-state transformations that were previously mentioned (recovery, recrystallization and grain growth), with the amount of necessary heat for these transformations to occur being lower with higher stored strain energy.

To further understand the impact of the welding process on the existing phases, high energy synchrotron X-ray diffraction was used to scan the sample. Representative X-ray diffraction patterns of the base material, heat affected and fusion zones are depicted in Fig. 2. Most of the low intensity diffraction peaks correspond to Cr-Mn-based oxides and are observed all along the joint. These oxides are easily formed in the Co-Cr-Fe-Mn-Ni system due to potential contamination of the raw material and oxidation during the casting process of the base material, as detailed in [24]. In the fusion zone, the higher temperatures experienced by the material further exacerbate the potential for oxidation to occur, which is aided by the strong affinity of both Cr and Mn with O [25], which explains the presence of these oxides at this location of the joint. Rietveld refinement of the diffraction data revealed that the oxides volume fraction in both the base material and heat affected zone is ≈ 2.5%, while in the fusion zone reaches ≈ 3.1%, with this increase justified by the extremely high temperatures developed at this location. In both the base material and heat affected zone (refer to Fig. 2(a) and Fig. 2(b), respectively) aside from the Cr-Mn oxides, these regions are composed by a disordered FCC phase, as typical of this material. In the fusion zone, the composition change induced by the addition of the 308 stainless steel filler material leads to present of other phases. In fact, aside from the previously identified disordered FCC phase and oxides, the fusion zone shows evidence of a disordered BCC (≈ 2.17%) and σ phases (≈ 0.77%).

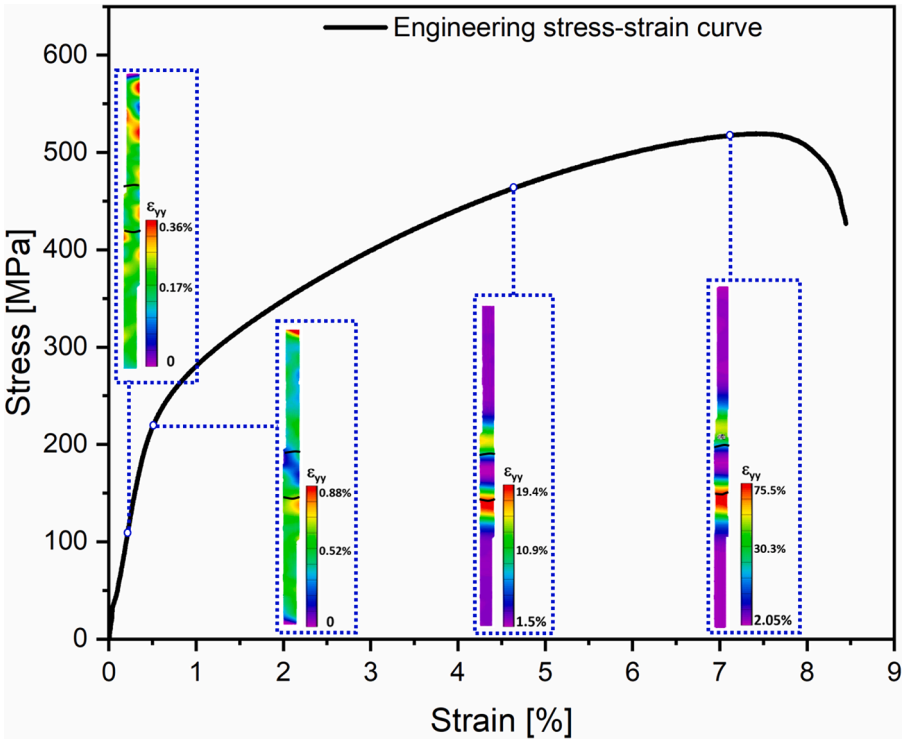

Fig. 5. Engineering stress-strain curve of the gas metal arc welded CoCrFeMnNi joints with ER308LSi filler material, with DIC snapshots obtained at different loading steps during loading until failure.

To further investigate the effect of dilution of the filler material on the solidification phases and solidification temperatures range, the Scheil-Gulliver model was used considering dilution steps of 1%. These results are detailed in Fig. 3.

When the dilution ratio ranges between 0 and 18% and 35 to 61%, the predicted solidification paths are Liquid + FCC → Liquid + BCC + FCC and Liquid + FCC → Liquid + FCC + σ, respectively. Thus, for these ranges of dilution, two phases are predicted to be formed. For the 19 to 34% range, FCC, BCC and σ phases are predicted, but equally contain two different solidification paths, Liquid + FCC → Liquid + BCC + FCC → Liquid + FCC + σ and Liquid + FCC → Liquid + BCC + FCC → Liquid + BCC + FCC + σ → Liquid + FCC + σ. When the dilution is above 60%, only FCC phase is predicted and the solidification path is Liquid → FCC. It is thus evident that the formation of σ and BCC phases are closely related to the dilution ratio: when the 308 filler is dominant, two (FCC and BCC) or three phases (FCC, BCC and σ) are expected in the fusion zone.

Although not shown here, the BCC phase is Fe- and Cr-rich, with its molar content ranging between 36.63 to 50.10% and 34.84 to 35.54%, respectively, depending on the dilution ratio. Since these elements are predominant in the filler material, it is thus clear the role of dilution on the potential formation of the BCC phase. The formed σ phase will be rich in both Cr (37.41 to 42.29 at.%) and Fe (28.70 to 37.13 at.%), as well as in Mn (9.01 to 18.37 at.%), again, depending on the fusion zone dilution.

Attention must also be paid to Mo, which composes the 308 filler material. Mo can promote the transformation from a single FCC phase structure to a mixture of FCC and BCC phases, while favoring the formation of σ phase in the Co-Cr-Fe-Mn-Ni system [26,27]. From our thermodynamic calculations, molar percentages of 1.81 to 1.87% and 2.81 to 3.07% of Mo can promote the formation of BCC and σ phases, respectively. These thermodynamic predictions are validated by the diffraction data previously presented.

The solidification temperature range of fusion-based welded joints has a significant effect on the cracking susceptibility. As can be seen in Fig. 3, the solidification temperature ranges from 154 to 171 °C. Although mixing of the base material and 308 filler wire changes the solidification temperature range of the molten pool, it does not vary considerably. Nevertheless, it still has a clear correlation with the number of phases being formed. In the relatively high solidification temperature range, only FCC or FCC + BCC are predicted, while FCC + σ are predicted in the lower solidification temperature range.

Fig. 4(a) and b) depict the hardness mapping of the welded joint and a line scan obtained at the middle height, respectively. Fig. 4(c) presents the average grain size variation in the base material, heat affected zone and fusion zone.

The as-rolled base material has the highest hardness, averaging 408 HV0.5 (region 1). Upon entering the heat affected zone, a continuous decrease in hardness is observed when progressing toward the fusion zone interface. While in the low temperature heat affected zone the hardness decreases to 408 HV0.5, in the high temperature side the drop is more significant to 151 HV0.5. This decrease in hardness is related to the effect of the weld thermal cycles on the microstructure condition, where recrystallization and grain growth promote to a decrease in hardness. Evidence of grain growth within the heat affected zone towards the fusion boundary is further evidenced in Fig. 4(c) and is in good agreement with the hardness evolution detailed in Fig. 4(a) and (b). Upon entering in the fusion zone (region 3), the hardness reaches its lowest value at ≈ 142 HV0.5, which is similar to that commonly observed in cast CoCrFeMnNi alloys [9]. Thus, although BCC and σ are formed in this region, with σ typically being a strengthening phase [28], its low volume fraction (0.77%) and very large grain structure of the FCC phase is not conducive to an evident increase in hardness. Moreover, the modification of the chemical composition of the fusion, via dilution, is not strong enough to induce solid solution strengthening compared to the equiatomic CoCrFeMnNi high entropy alloy.

Fig. 5 details a representative engineering stress-strain curve for the CoCrFeMnNi joints, and different DIC strain maps obtained at different stress/strain conditions. The yield strength, ultimate tensile strength and elongation of the welded joint were 225 MPa, 517 MPa and 8.4%,

respectively. While the elongation of the welded joint is only slightly lower than that of the base material [23] (8.4 vs 9.4%), the tensile strength significantly decreases (517 vs 945 MPa).The relatively poorer mechanical performance of the welded joint compared to the base material, while still being able to be considered for structural applications, is explained considering both the microstructure features and DIC maps obtained: the fusion zone, with its lower hardness and extremely large grain size, will promote significant strain concentration, while in the non-welded material the load is more uniformly distributed. Owing to this strain concentration in the fusion zone, the remaining parts of the joint are less strained and the overall deformation sustained is lower than in the original base material. Nonetheless, the local strain experienced by the fusion zone can reach up to ≈ 75% suggesting that this region is highly ductile. Future work will assess how different post-weld heat treatments can be used to improve the mechanical response of these welded joints.

This work combined advanced material characterization, thermodynamic simulations and mechanical testing to provide a comprehensive analysis of the microstructure evolution and mechanical properties of gas metal arc welding CoCrFeMnNi joints obtained with ER308LSi filler material. The results show that the prestored strain energy in the as-rolled base material and the weld thermal cycle are the main driving forces for recrystallisation and grain growth occurring in the heat affected zone, and in turn, such solid-state transformations are the direct causes for the hardness drop in this region. A chemical composition gradient caused by the dilution of the filler material is closely related to the phase structure that is formed in the fusion zone. Mechanical testing detailed that the joints can be considered for structural application, despite fracture occurred in the fusion zone region.

Declaration of Competing Interest

The authors declare that they have no known competing financial interests or personal relationships that could have appeared to influence the work reported in this paper.

Acknowledgments

JS, JGL and JPO acknowledge Fundação para a Ciência e a Tecnologia (FCT - MCTES) for its financial support via the project UID/00667/2020 (UNIDEMI). JPO acknowledges funding by national funds from FCT - Fundação para a Ciência e a Tecnologia, I.P., in the scope of the projects LA/P/0037/2020, UIDP/50025/2020 and UIDB/50025/2020 of the Associate Laboratory Institute of Nanostructures, Nanomodelling and Nanofabrication – i3N. JS acknowledges the China Scholarship Council for funding the Ph.D. grant (CSC NO. 201808320394). JGL acknowledges Fundação para a Ciência e a Tecnologia (FCT-MCTES) for funding the Ph.D. Grant 2020.07350.BD. This work was supported by the National Research Foundation of Korea (NRF) grant funded by the Korea government (MSIP) (NRF-2022R1A5A1030054). The authors acknowledge DESY (Hamburg, Germany), a member of the Helmholtz Association HGF, for the provision of experimental facilities. Beamtime was allocated for proposal I-20210899 EC. The research leading to this result has been supported by the project CALIPSOplus under the Grant Agreement 730872 from the EU Framework Programme for Research and Innovation HORIZON 2020.

References

[1] B. Cantor, I.T.H. Chang, P. Knight, A.J.B. Vincent, Mater. Sci. Eng. 375–377 (2004) 213–218.
[2] J.W. Yeh, S.K. Chen, S.J. Lin, J.Y. Gan, T. Chin, T.T. Shun, C. Tsau, S.Y. Chang, Adv. Eng. Mater. 6 (2004) 299–303.
[3] B. Cantor, Prog. Mater Sci. 120 (2021), 100754.
[4] H. Jiang, H. Zhang, T. Huang, Y. Lu, T. Wang, T. Li, Mater. Des. 109 (2016) 539–546.
[5] O.N. Senkov, G.B. Wilks, J.M. Scott, D.B. Miracle, Intermetallics 19 (2011) 698–706.
[6] Y. Shi, B. Yang, P. Liaw, Metals (Basel) 7 (2017) 43.
[7] C.L. Wu, S. Zhang, C.H. Zhang, H. Zhang, S.Y. Dong, J. Alloy. Compd. 698 (2017) 761–770.
[8] I. Basu, V. Ocelík, J.T.M. De Hosson, J. Mater. Res. 33 (2018) 3055–3076.
[9] J. Gu, M. Song, Scr. Mater. 162 (2019) 345–349.
[10] M. Laurent-Brocq, A. Akhatova, L. Perrière, S. Chebini, X. Sauvage, E. Leroy, Y. Champion, Acta Mater. 88 (2015) 355–365.
[11] G. Laplanche, A. Kostka, O.M. Horst, G. Eggeler, E.P. George, Acta Mater. 118 (2016) 152–163.
[12] M.G. Jo, H.J. Kim, M. Kang, P.P. Madakashira, E.S. Park, J.Y. Suh, D.I. Kim, S. T. Hong, H.N. Han, Met. Mater. Int. 24 (2018) 73–83.
[13] N. Kashaev, V. Ventzke, N. Stepanov, D. Shaysultanov, V. Sanin, S. Zherebtsov, Intermetallics 96 (2018) 63–71.
[14] H. Nam, C. Park, C. Kim, H. Kim, N. Kang, Sci. Technol. Weld. Join. 23 (2018) 420–427.
[15] Z. Wu, S.A. David, Z. Feng, H. Bei, Scr. Mater. 124 (2016) 81–85.
[16] Z. Wu, S.A. David, D.N. Leonard, Z. Feng, H. Bei, Sci. Technol. Weld. Join. 23 (2018) 585–595.
[17] H. Nam, B. Moon, S. Park, N. Kim, S. Song, N. Park, Y. Na, N. Kang, Sci. Technol. Weld. Join. 27 (2022) 33–42.
[18] N.K. Adomako, G. Shin, N. Park, K. Park, J.H. Kim, J. Mater. Sci. Technol. 85 (2021) 95–105.
[19] H. Do, S. Asadi, N. Park, Mater. Sci. Eng. 840 (2022), 142979.
[20] J.P. Oliveira, A. Shamsolhodaei, J. Shen, J.G. Lopes, R.M. Gonçalves, M. de Brito Ferraz, L. Piçarra, Z. Zeng, N. Schell, N. Zhou, H. Seop Kim, Mater. Des. 219 (2022), 110717.
[21] A.P. Hammersley, J. Appl. Crystallogr. 49 (2016) 646–652.
[22] L. Lutterotti, R. Vasin, H.R. Wenk, Powder Diffr. 29 (2014) 76–84.
[23] J.P. Oliveira, T.M. Curado, Z. Zeng, J.G. Lopes, E. Rossinyol, J.M. Park, N. Schell, F. M. Braz Fernandes, H.S. Kim, Mater. Des. 189 (2020), 108505.
[24] B. Gludovatz, A. Hohenwarter, D. Catoor, E.H. Chang, E.P. George, R.O. Ritchie, Science 345 (2014) 1153–1158.
[25] Y.K. Kim, Y.A. Joo, H.S. Kim, K.A. Lee, Intermetallics 98 (2018) 45–53.
[26] Y. Zhao, X. Zhang, H. Quan, Y. Chen, S. Wang, S. Zhang, J. Alloy. Compd. 895 (2022), 162709.
[27] G. Qin, R. Chen, H. Zheng, H. Fang, L. Wang, Y. Su, J. Guo, H. Fu, J. Mater. Sci. Technol. 35 (2019) 578–583.
[28] K. Cho, Y. Fujioka, T. Nagase, H.Y. Yasuda, Mater. Sci. Eng. 735 (2018) 191–200.